The Astrophysical Journal, 857:90 (15pp), 2018 April 20 https://doi.org/10.3847/1538-4357/aab6b7

Study of Three-dimensional Magnetic Structure and the Successive Eruptive Nature of Active Region 12371

P. Vemareddy[1] and P. Demóulin[2]
[1] Indian Institute of Astrophysics, Koramangala, Bengalure-560034, India; vemareddy@iiap.res.in
[2] Observatoire de Paris, LESIA, Meudon, France
Received 2017 November 6; revised 2018 February 19; accepted 2018 March 12; published 2018 April 18

Abstract

We study the magnetic structure of a successively erupting sigmoid in active region 12371 by modeling the quasi-static coronal field evolution with nonlinear force-free field (NLFFF) equilibria. Helioseismic and Magnetic Imager/*Solar Dynamic Observatory* vector magnetograms are used as input to the NLFFF model. In all eruption events, the modeled structure resembles the observed pre-eruptive coronal sigmoid and the NLFFF core field is a combination of double inverse-J-shaped and inverse-S field lines with dips touching the photosphere. Such field lines are formed by the flux cancellation reconnection of opposite-J field lines at bald-patch locations, which in turn implies the formation of a weakly twisted flux-rope (FR) from large-scale sheared arcade field lines. Later on, this FR undergoes coronal tether-cutting reconnection until a coronal mass ejection is triggered. The modeled structure captured these major features of sigmoid-to-arcade-to-sigmoid transformation, which is reoccuring under continuous photospheric flux motions. Calculations of the field line twist reveal a fractional increase followed by a decrease of the number of pixels having a range of twist. This traces the buildup process of a twisted core field by slow photospheric motions and the relaxation after eruption, respectively. Our study infers that the large eruptivity of this AR is due to a steep decrease of the background coronal field meeting the torus instability criteria at a low height (≈40 Mm) in contrast to noneruptive ARs.

Key words: Sun: corona – Sun: coronal mass ejections (CMEs) – Sun: evolution – Sun: filaments, prominences – Sun: flares – Sun: magnetic fields

1. Introduction

It is now accepted that the source of energy for all solar activity is from magnetic fields. Active regions (ARs) are higher concentrations of magnetic-field regions often associated with violent activity, like jets, flares, coronal mass ejections (CMEs), etc. In X-rays and EUV observations, these regions are sometimes seen with a sigmoid structure (Rust & Kumar 1996; Gibson et al. 2002) situated over the central polarity inversion line (PIL). The sigmoid structure is either forward or inverse-S-shaped. Several CMEs have launched from these sigmoidal ARs and hence a sigmoid is one of the most important precursor structures for solar eruptions (Manoharan et al. 1996; Hudson et al. 1998; Canfield et al. 1999, 2007). Two types of sigmoids were reported: transient and long-lived. Transient sigmoids are sharp and bright and they usually become clearly noticeable only for a short time before eruption, while long-lived ones appear more diffuse and can survive for several hours, even days (Pevtsov 2002; McKenzie & Canfield 2008).

The magnetic structure of sigmoids was described as sheared arcade and flux rope (FR) topology (Moore et al. 2001). In the sheared arcade model, the two magnetic elbows are sheared field lines that are located nearby on both sides of the PIL in the central part of the configuration. In the FR scenario, a magnetic FR is embedded in a stabilizing potential envelope field (Moore & Roumeliotis 1992; Hood & Priest 1979; Titov & Démoulin 1999). How do these sigmoids become eruptive? Magnetic reconnection (resistive instability) plays the prime role in the sheared arcade model as opposed to ideal MHD instability in the FR model in triggering the eruption (Antiochos et al. 1999; Moore et al. 2001; Amari et al. 2003; Török & Kliem 2005; Gibson et al. 2006). The interface separating a coronal FR from its ambient field usually forms a sigmoidal shape when observed from above and FRs are naturally invoked in different models of sigmoids (Titov & Démoulin 1999; Gibson et al. 2006; Bobra et al. 2008; Savcheva & van Ballegooijen 2009). Sigmoids are considered to result from enhanced current dissipation in thin sheets, which accumulate hot plasma along corresponding shaped field lines (Gibson et al. 2002; Janvier 2017).

During the evolution of an AR, magnetic energy is built up (during several hours or even days) in the corona due to flux emergence and photospheric motions (Schrijver 2009). The energy is stored in a nonpotential field associated with large-scale electric currents (Priest & Forbes 2002; Aulanier et al. 2010).

A topological analysis of magnetic structures, constructed from analytic configurations, predicted that the current sheets form along magnetic interface layers, called separatrices, as well as along their generalization, called quasi-separatrix layers (Priest & Démoulin 1995; Priest & Forbes 2000; Aulanier et al. 2005). The connectivity of field lines is discontinuous for separatrices, while it changes drastically along QSLs (Demoulin et al. 1996). In an analytical force-free FR model embedded in an arcade field, Titov & Démoulin (1999) showed that in the process of the FR emerging rigidly into the corona, a separatrix surface, touching the photosphere at a so-called bald patch (BP, $\boldsymbol{B} \cdot \nabla B_z|_{\rm PIL} > 0$), is present along the PIL section during the earlier phase of emergence. The BP separatrix surface has a generic S-shape when viewed from the top, similar to sigmoid shape. In the later phase of emergence, the S-shaped BP separatrix is transformed into a double J-shaped QSL. The topological analysis of the FR eruptions found cospatial flare ribbons with hook-shaped QSLs (Démoulin et al. 1996; Williams et al. 2005; Janvier et al. 2014; Zhao et al. 2016),

leading to the extension of a 2D version of the standard model to 3D (Janvier et al. 2015).

In decaying ARs, the sigmoids were reported to have been formed by flux cancellation induced by converging motions of magnetic elements toward PIL (Green & Kliem 2009; Tripathi et al. 2009; Vemareddy & Mishra 2015). Helical field lines are formed by the reconnection of sheared field lines (Pneuman 1983; van Ballegooijen & Martens 1989). Numerical simulations have shown FR formation under the canceling magnetic flux scenario (e.g., Amari et al. 2003). On the other hand, numerical models that produce FRs also rely on the magnetic flux emergence of twisted FRs that originate from the convection zone and rise through the photosphere (Magara 2001; Fan & Gibson 2004; Gibson et al. 2004; Archontis et al. 2009; Hood et al. 2012). In these models, as the FR emerges, a filamentary current sheet forms, reconnection occurs, and a new coronal FR is formed. When integrated along the local vertical, the current sheet appears as a sigmoid.

It is not presently possible to observationally study the 3D magnetic structure of AR. Therefore, one must rely on models based on field measurements at the photosphere as the lower boundary condition. A nonlinear force-free field (NLFFF) model is typically used to reconstruct the pre-eruptive coronal field (Valori et al. 2005; Wiegelmann 2008; De Rosa et al. 2009; Savcheva & van Ballegooijen 2009; Jiang & Feng 2012). This is justified by the low-β coronal condition. However, this is not realized at the photospheric level and a preprocessing procedure is applied to drive the lower boundary toward the force-free condition (Wiegelmann et al. 2006). Moreover, the photospheric flow speed is very slow, typically well below 1 km s^{-1} (Vemareddy et al. 2012), compared to the speed of the coronal field relaxing to equilibrium, which is several hundred km s^{-1}. Therefore, the coronal field evolution, driven by slow photospheric motion, can be approximated as a quasi-static evolution and it is modeled by the time sequence of successive static force-free equilibria. This enables us to study the buildup of pre-eruptive 3D structure, like a sigmoid, then to find hints of the most appropriate configurations leading to eruptions (e.g., Savcheva et al. 2012a; Sun et al. 2012, 2013; Jiang et al. 2014; Vemareddy & Wiegelmann 2014; Vemareddy et al. 2016).

In the present article, we construct the 3D magnetic structure of a sigmoidal AR with the NLFFF model and study the pre-eruptive configuration of observed CMEs. For this purpose, we employ vector magnetic-field measurements at the photospheric level obtained from the *Helioseismic and Magnetic Imager* (HMI; Schou et al. 2012) on board the *Solar Dynamic Observatory* (*SDO*; Pesnell et al. 2012). We study AR 12371, which produced successive fast CMEs during its disk transit. In EUV observations, the pre-eruptive configuration of all CMEs is a sigmoid. Being CME productive, we study how the sigmoid developed repeatedly and how it was eventually brought to instability. This case is in contrast with most previous studies of decaying ARs, where only one single sigmoid eruption was present during the observation window (Démoulin et al. 2002; Green & Kliem 2009; Green et al. 2011; Vemareddy & Mishra 2015). Based on the time sequence of these static NLFFF extrapolations, we focus on studying (1) the sigmoid buildup in the pre-eruptive configuration, (2) the build up of the coronal electric currents and their dissipation during eruption, (3) the magnetic energy, (4) the evolution of field line twist distribution, and (5) the role of the background field in driving the eruptions. We outline the observations during CME onset in Section 2. Results of the above studies are described in Section 3. A summary and a discussion of the results are given in Section 4.

2. Outline of Observations and Context of the Study

AR 12371 is an AR that formed before its appearance at the eastern limb. It produced successive fast CMEs in the span of its disk transit (2015 June 18–25). A recent study of this AR by Vemareddy (2017) presented a detailed analysis of the magnetic evolution in relation to the initiating mechanism of the successive CMEs. Here we give a brief outline of earlier results in the context of this study. Observations of the Sun register the initiation times of four eruptions as 15:05 UT on 18 (SOL2015 June 18T15:05, CME1), 00:45 UT on 21 (SOL2015 June 21T00:45, CME2), 16:15 UT on 22 (SOL2015 June 22T16:15, CME3), and 07:30 UT on 25 (SOL2015 June 25T07:30, CME4) of 2015 June, respectively, by the commencement of enhancing EUV brightening associated with fast structural changes. Subsequently, the disk integrated GOES X-ray light curve (Figure 1) delineates that the CMEs are associated with long-duration M-class flares starting from 18/16:25 UT, 21T02:00 UT, 22T17:39 UT, and 25T08:02 UT, respectively. These CMEs emerged from the C2 field of view at 18/17:24 UT, 21T02:36 UT, 22T18:36 UT, and 25T08:00 UT, respectively. All four CMEs are fast (>1000 km s^{-1}) in the LASCO field of view.

In Figure 2, we show simultaneous multiwavelength observations, taken from different instruments, of the AR during the onset phase of CMEs. Different wavelength snapshots at different times are selected to best show the observed structures. All image panels are aligned, accounting for spatial scales. In the first row, we plot line-of-sight magnetograms obtained from HMI. The AR successive passage reveals the presence of leading negative flux (N1) with a following bipole with negative (N2, N3) and positive (P1, P2) flux regions. The inner bipole (N2, N3) is seen with large shear and converging motions (see Figure 6 of Vemareddy 2017) with respect to (P1, P2), forming sheared PIL indicated with a blue curve. The field distribution of (N2, N3) becomes diffused and disintegrated in successive days while the leader polarity is increasingly separated from the following polarity.

In the second row of Figure 2, we plot GONG-Hα images. They show the presence of a dark filament between leading and following sunspots before the eruptions. In tandem, 304 Å observations from the Atmospheric Imaging Assembly (AIA; Lemen et al. 2012) are in support of H$_\alpha$, showing cospatial existence of continuous filament channel. A filament is present on the PIL portion southward of the AR. It could only be related to the faint magnetic field observed southward of the AR and be irrelevant to the eruption, since no apparent change of the filament can be recognized after the commencement of EUV brightening from the time sequences associated with Figure 2. The 131 Å channel of AIA (fourth row panels) evidences a sheared loop morphology comparable to those previously reported in other ARs (e.g., Moore et al. 2001). They consist of two opposite-J-shaped loops outlined by L1 and L2 (dashed orange curves) identified from a sequence of images. We call them magnetic elbows. The inner ends of these loops are nearby and cross each other with a sharp interface low over the PIL. Finally, the composite images prepared from the hot AIA channels are shown in the bottom row of Figure 2.

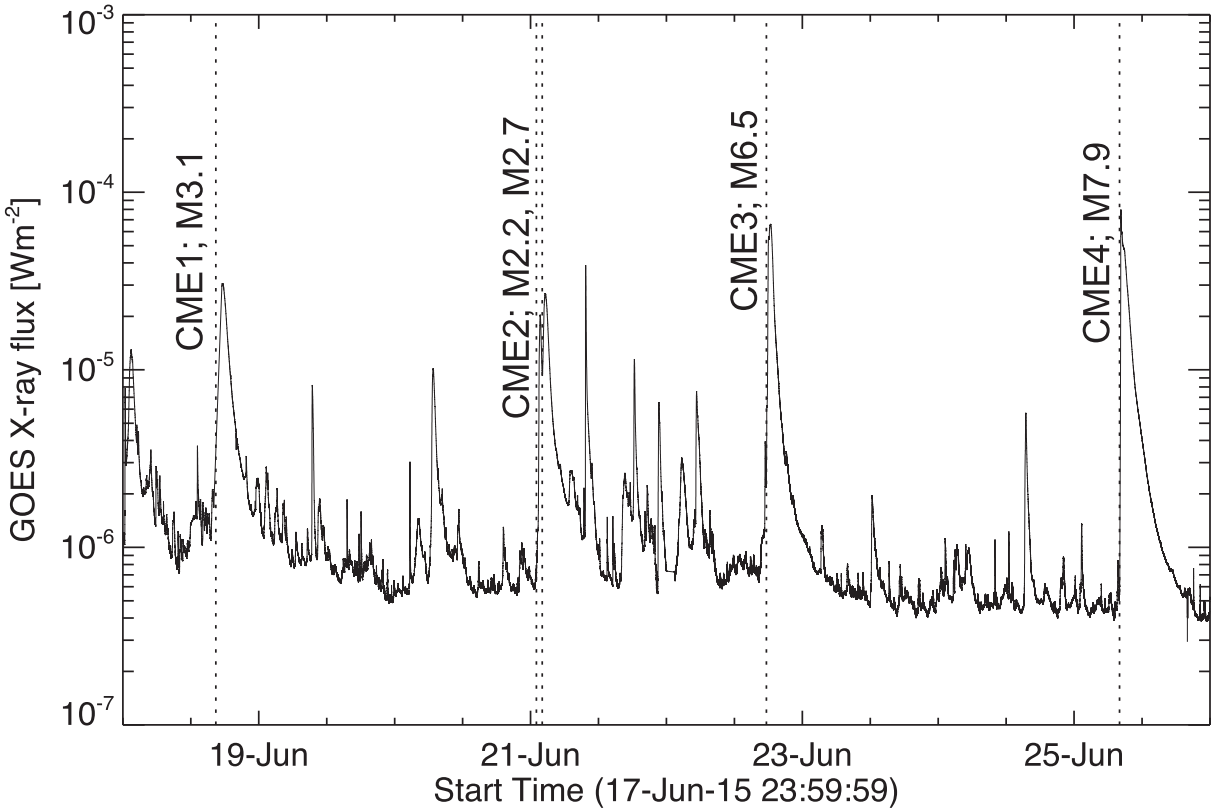

Figure 1. Disk integrated *GOES* X-ray flux (1–8 Å) during 2015 June 18–25. Vertical dotted lines mark the initial times of CME-associated M-class flares from AR 12371.

They provide evidence for continuous sigmoidal structure (labeled L3) during the initiation of all four CMEs.

The configuration outlined by L1 and L2, especially in the three last events, is typically found in models with a sheared core (e.g., Antiochos et al. 1994; Aulanier et al. 2010). In the tether-cutting scenario, magnetic reconnection is initiated at the interface of L1 and L2's closest legs when converging motions push the legs against each other. The large-scale reconnected field lines have a shape comparable to L3. This reconnection progressively transforms sheared field lines, such as those observed with L1 and L2, to twisted field lines, as outlined with L3. As reconnection proceeds further, the FR bulges and rises in height. In numerical simulations (Aulanier et al. 2010), once the FR is too high, the configuration becomes unstable and the FR escapes the coronal closed field environment into the outer corona as a CME. The AIA composite images (fifth row panels in Figure 2) evidence this FR (labeled as L3) during the initiation of CMEs.

The study of magnetic-field evolution (please refer to Figure 7 in Vemareddy 2017) implies decreasing magnetic flux in both AR polarities, which is an indication of magnetic flux cancellation. Velocity field of flux motions derived from DAVE4VM (Schuck 2008) show the shear and converging motions, which are in support of the above tether-cutting reconnection, within the inner bipolar regions (Figure 3). These motions were suggested to be prime factors of the flux cancellation and the net flux decrease (Chae et al. 2002, 2004). Under this flux evolution, the net current and α_{av} (mean twist parameter of magnetic-field) show an increasing trend until June 22. This is an indication of build up of nonpotentiality (Martin 1998; Wang & Muglach 2007). Furthermore, with these observational findings of magnetic evolution, Vemareddy (2017) described that the repeated sigmoid formation and its eruption by successive CMEs is a result of energy storage and release by persistent shearing and converging motions. With monotonous injection of negative helicity, the corona overaccumulates helicity and expels excess helicity by CME. Predominant influx of helicity of either sign over time is the key for the formation of coronal sigmoid or FR, which would be initiated to ejection by ideal or nonideal instability (Moore et al. 2001; Török & Kliem 2005). Using vector magnetic field observations at the photosphere, in the present article, we study the different aspects in magnetic structure of the pre-eruptive sigmoid with NLFFF models.

3. Results

3.1. Nonlinear Force-free Modeling of the AR Field

The AR magnetic structure is reconstructed by performing NLFFF extrapolation of the observed photospheric vector magnetic field (Bobra et al. 2014; Hoeksema et al. 2014). This procedure minimizes a volume integral, including a linear combination of the Lorentz force and of the magnetic field divergence (Wiegelmann 2004; Wiegelmann & Inhester 2010). The field of view of the boundary field covers the full AR such that flux is nearly balanced over the entire time interval. During all four CME events, the flux imbalance is less than 8%. To further satisfy the force-free conditions, the magnetic field components are subjected to a preprocessing procedure (Wiegelmann et al. 2006). Next, we rebinned the observations to 1 arcsec per pixel. In order to weaken the effects of the

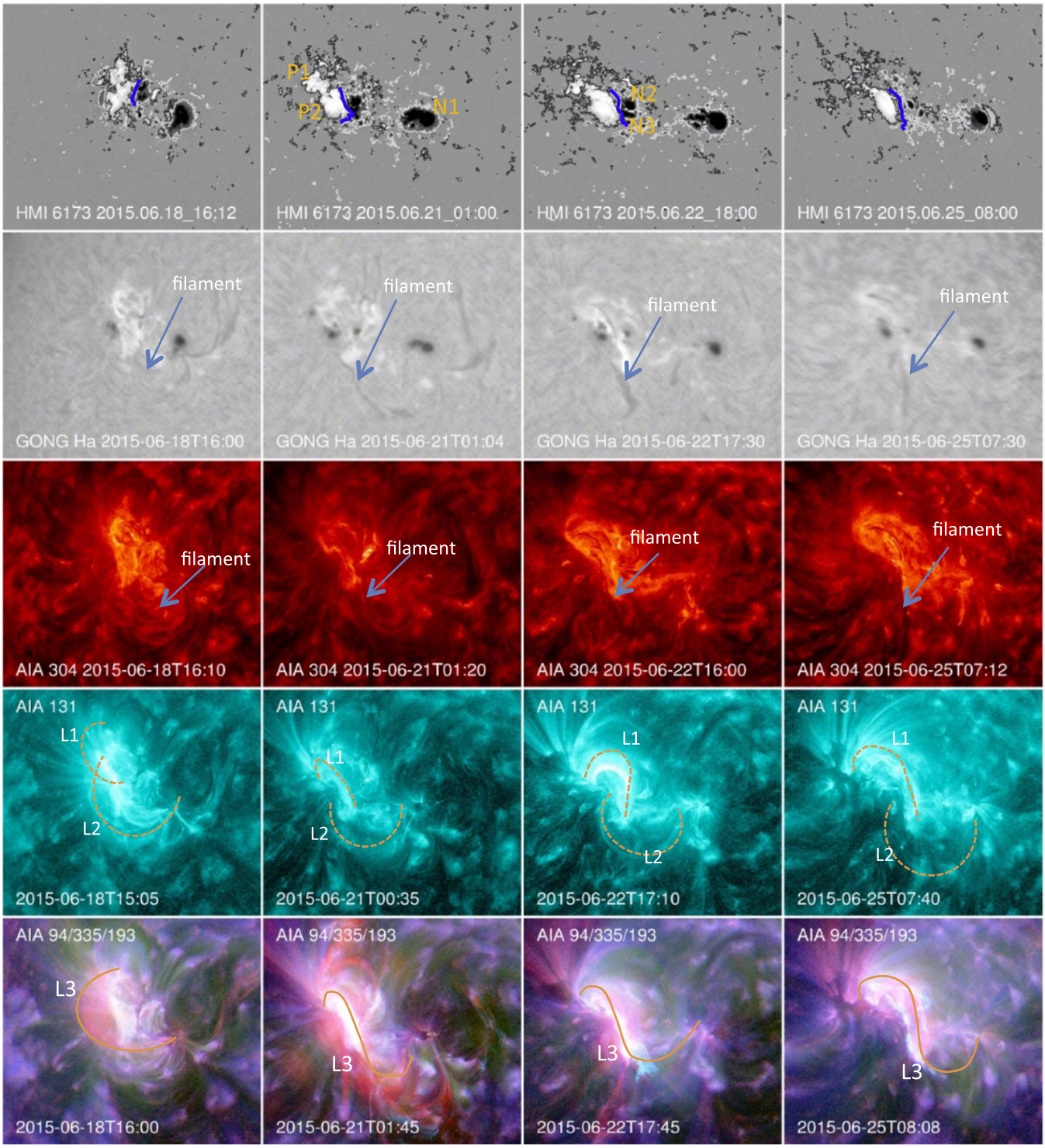

Figure 2. Multiwavelength observations of the AR 12371 during the initiation of four CMEs shown in the four columns. Each panel of the same event has the same field of view. First row: HMI line-of-sight magnetic-field maps with labeled polarity regions. The blue curve is the main PIL. Second row: GONG Hα observations showing traces of chromospheric filaments and sunspots (related to HMI magnetic polarities). Third row: AIA 304 Å observations showing the presence of a filament (indicated by the blue arrow) before the onset of the CME eruption. Fourth row: AIA 131 Å observations before eruptions. In particular, they show the coronal loop sets as magnetic elbows and are traced with dashed curves L1 and L2 by inspecting time series of images. In these observations, the precursor brightening related to slow tether-cutting reconnection is seen with L1. Fifth row: composite images of coronal observations in AIA 94 Å (red), 335 Å (green), and 193 Å (blue) passbands. The loop set L3 (outlined with an orange curve) is understood as the dynamic reconnection product of L1 and L2. See Section 2 for more details.

lateral boundaries, the observed boundary is inserted in an extended field of view and computations are performed on a uniformly spaced computational grid of $512 \times 512 \times 256$, representing physical dimensions of $373 \times 373 \times 186\,\mathrm{Mm}^3$. To reduce the effect of pseudo top and side boundaries on the evolving interior field, a boundary wall (of width 64 grid points) of the cosine weighting function is used in the function that is minimized.

The NLFFF code is initiated with a 3D potential field constructed from the vertical field component of the observed

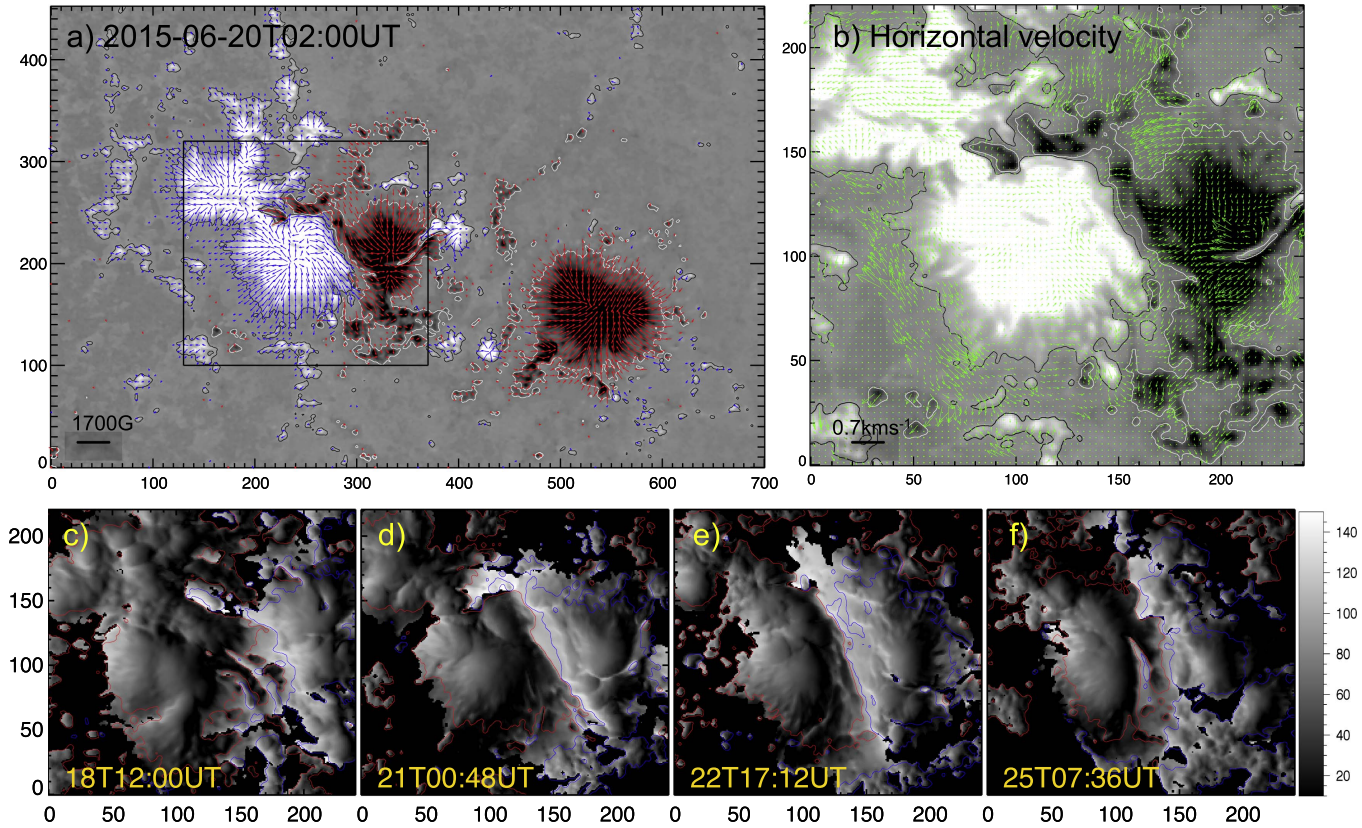

Figure 3. (a) HMI Vector magnetogram of AR 12371 on June 20. Blue/red arrows represent the horizontal field. Background is the vertical field image with contours at ±150 G. (b) Tracked horizontal velocity field on the vertical field map. The field of view covers the inner bipolar region as is shown with the rectangular box in panel (a). Careful inspection implies a slow shear and converging motion between the opposite polarity regions. (c)–(f) Maps of shear angle in the inner bipolar region covered by the rectangular box in (a) (see the color bar). Contours (red/blue) of B_z at ±150 are overlaid. In the vicinity of the PIL, both the positive and negative polarities have sheared locations greater than 45°. Finally, as a result of flux cancellation along the PIL and dispersion of the photospheric field, the polarity regions decayed in area from June 18 to 25. In all panels, the axis units are in pixels of 0.5 arcsec.

field (Gary 1989). After introducing the photospheric vector magnetic field at the lower boundary, the magnetic field is relaxed as much as possible to decrease both the Lorentz force and the divergence of the magnetic field. Typically, the observed photospheric field, even after processing, is not compatible with the NLFFF state, but it can be relaxed to a state with an average angle typically around 9° between the electric current and magnetic field vectors in the computational volume.

A typical vector magnetogram used in the NLFFF reconstruction is shown in Figure 3(a). The rectangular box covers the inner bipolar region. The horizontal velocity field, derived from the DAVE4VM method, indicates a large-scale convergence and shear motions of opposite polarities in the inner bipolar region, as displayed in panel (b). Under these motions, the field vectors are sheared where the angle between potential transverse field and the observed transverse field is non-zero. We measured the shear angle defined as the angle between the potential transverse field and the observed transverse field. In panels (c)–(f), these shear angle maps are displayed at different epochs of evolution. Both the positive and negative polarities have sheared locations greater than 45°. In particular, the negative polarity region is more sheared than the positive polarity region. The magnetic shear is especially important around the PIL in between (N2, N3) and (P1, P2) (See Figure 2 for polarity identification). Tracked magnetograms infer a southward motion of the negative polarity with respect to the positive polarity. This is the main origin of this shear region (Vemareddy 2017).

As pointed out by Moore et al. (2001), two likely factors for the eruption are the flux content of the sheared core field relative to the envelope field and the height at which the reconnection begins. The greater the reconnection height, the smaller the fraction of the core field that can be released as the eruption proceeds. We compute the shear angle in the inner bipolar region (rectangular box in Figure 3(a)) for the vector magnetograms recorded just before all three eruptions. In this bipolar region, we found that 20%, 30%, and 30% of pixels have greater than 45° shear angle, while the pixels with shear angle greater than 25° are 58%, 45%, and 48%, respectively, for the last three events. Alternatively, the numbers meet Moore et al's first criteria of excess flux content of sheared core field with a shear angle above 25°.

In Figure 4, we show the NLFFF magnetic structure just before the CMEs. Being located at E50°, the CME1 is excluded from further analysis due to severe projection effects. The field lines are selected according to the total current density ($|\boldsymbol{J}| = \frac{1}{\mu_0}(\nabla \times \boldsymbol{B})$) and the horizontal field component ($B_h = \sqrt{B_x^2 + B_y^2}$), i.e., the seed points are biased with large $|\boldsymbol{J}|$, B_h in a subvolume covering the inner bipolar region. This will ensure that we select field lines that outline most of the observed coronal loops (Figure 2). A color scheme according to B_h strength is applied for the field lines. The bottom plane is B_z

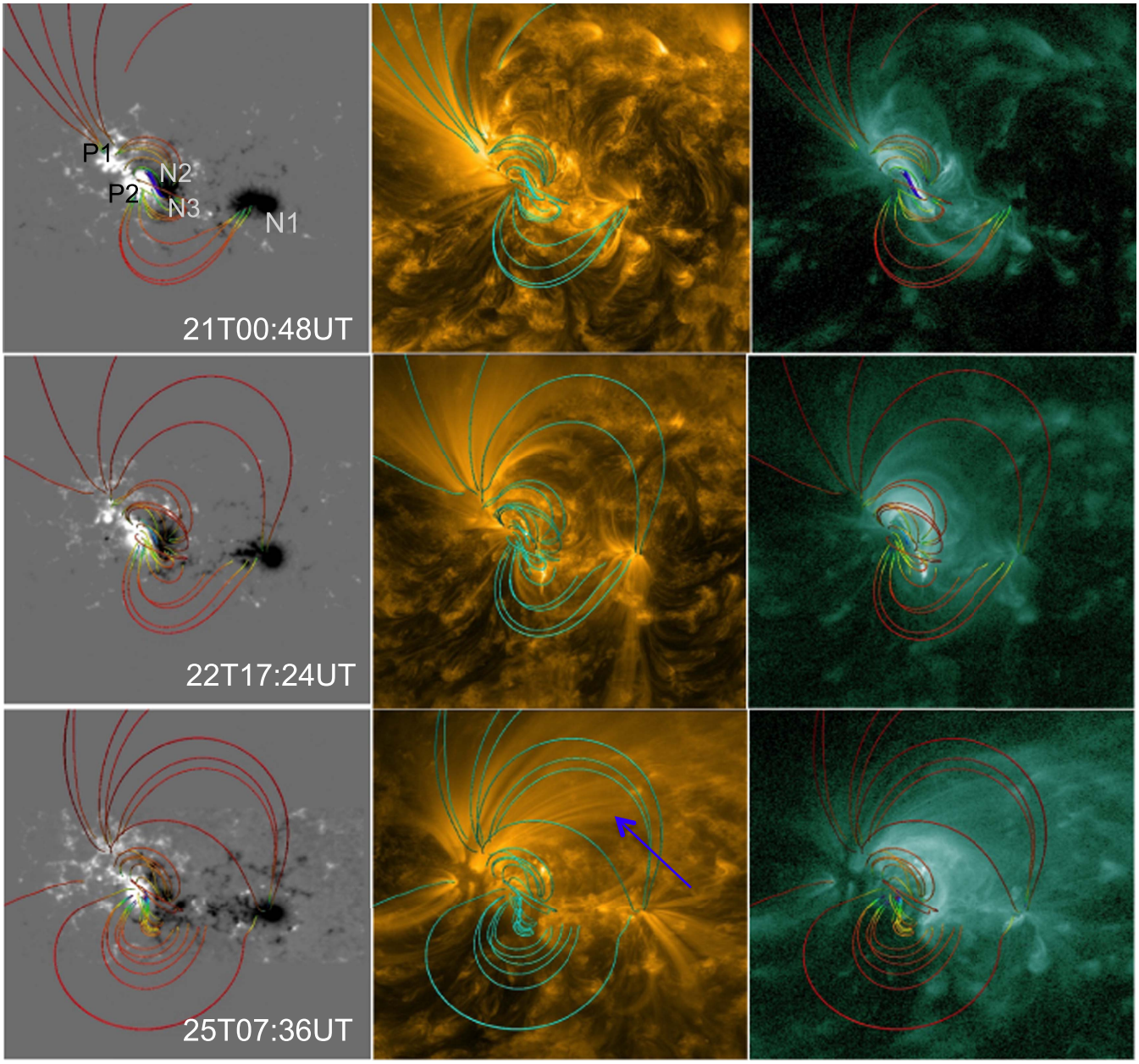

Figure 4. NLFFF magnetic structure of AR 12371 during the three eruption events. First column: field lines plotted on top of the photospheric magnetogram (B_z) with labeled polarity regions. The global structure is a sigmoid with two opposite-J-shaped sections and an inner sheared core. Second column: same field lines on AIA 171 Å images. The color scale is chosen in contrast to background images. Third column: same field lines on AIA 94 Å images. Hot plasma emission is mainly cospatial with the strongly sheared core. Note that for event 4 (bottom rows) the projection effects tend to deviate the model structure, especially the long field lines from the observed 171 Å loops indicated by the arrow. Field lines are color coded (blue (red): ∼1200 (2)G) with the horizontal field strength in height in columns 1 and 3.

in the first column panels. Field lines connecting the peripheral regions of P1 and N2 form one J-section loop set, and those connecting N1 and P2 form another J-section loop set. These two bundles of J-shaped field lines are formed by highly sheared arcades.

Owing to line-tied shearing motions of the foot points, the field lines near the PIL, in the AR center, are strongly sheared. They are enveloping field lines over the middle of the sigmoid. This sheared magnetic configuration, as shown in Figure 2, being further driven by converging motions of two opposite-J-sections, is expected to favor the formation of FR by tether-cutting reconnection (Titov & Démoulin 1999; Jiang et al. 2012; Savcheva et al. 2012a).

To compare this modeled magnetic structure to coronal observations, the same field lines are overplotted on EUV observations of coronae in 171 and 94 Å passbands (second and third column panels). The EUV loops are in global agreement with the NLFFF twisted structure in each panel (in agreement with previous results, Sun et al. 2012; Vemareddy & Wiegelmann 2014). Remarkably, the intense hot emission is mostly cospatial with the NLFFF sheared core. The sheared core is less compact for the last event on June 25 compared to others. This indicates a relaxed configuration after a sequence of eruptions and quasi-static evolution in between two events.

We note that the projection effects in the corona are greater than those in the photosphere. It is also notable that, being

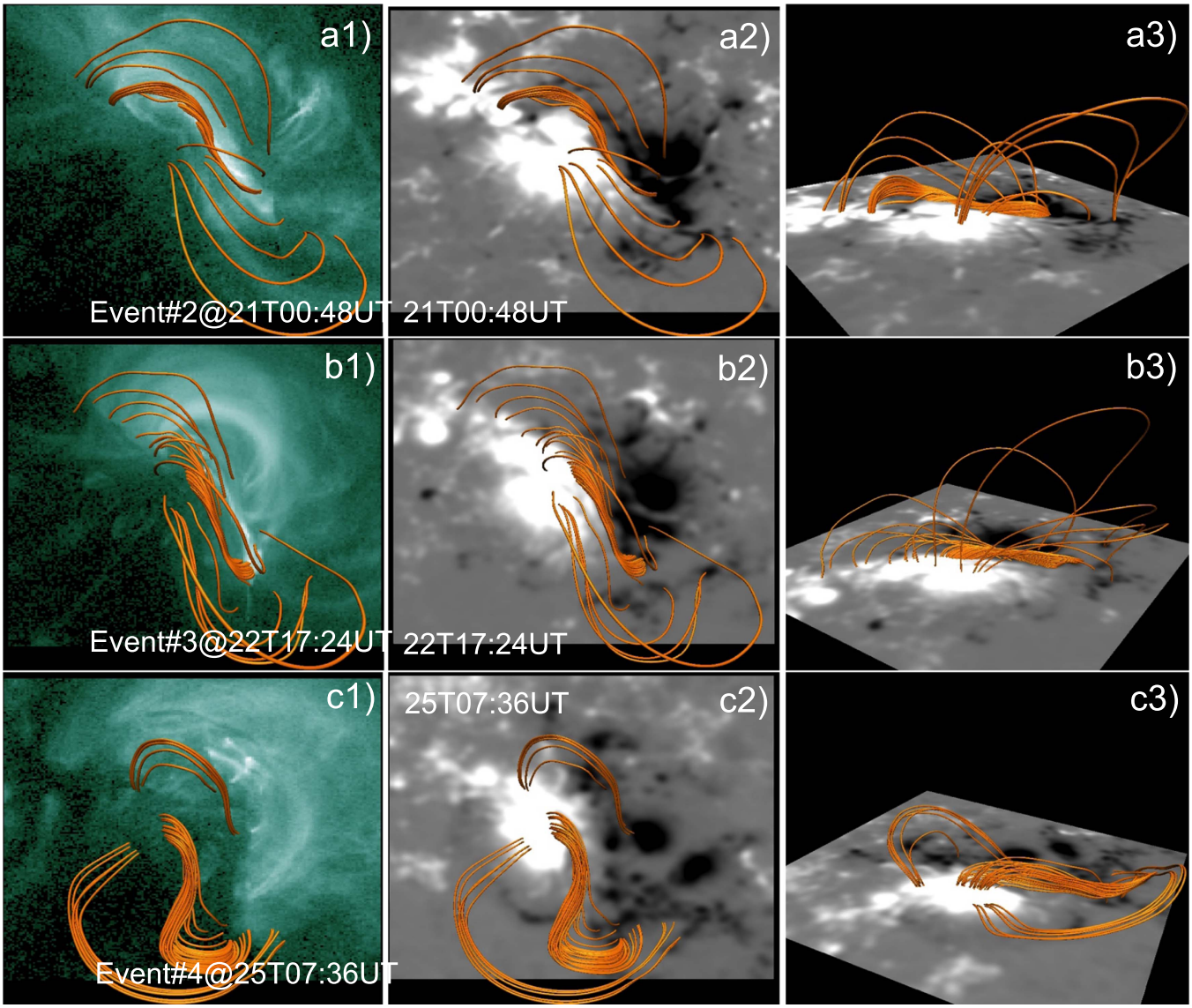

Figure 5. Field line shapes in the core and EUV observations (organized by rows). First column: field lines on EUV-94 images, showing a twisted field embedded in the large-scale sheared arcade. The twisted field is cospatial with EUV emission, whereas emission from the northern elbow comes from the high-lying potential field. (see also Figure 4). Second column: top view of the core field line structure. The photospheric B_z distribution observed at the same times is shown by gray levels in the background for all panels. Third column: perspective view of the same field lines showing the coronal extent of the sheared arcade

away from disk center, projection effects introduce some departures with large-scale loops, especially on June 25 (located at 40° west). However, the low-lying core structure is nearly reproduced because disk transformation from local to observer frames mostly takes into account these projection effects.

In a study of sigmoid eruption from another AR (AR 11283), Jiang et al. (2014) reported the FR formation by reconnection that was attached to photosphere at the bald patch (BP) until eruption. Following their analysis, we further discuss the eruption cases in AR 12371 as follows. In Figure 5, we examine the core field topology of the NLFFF structure. Field lines anchoring away from the PIL correspond to two J-sections with their arms farther apart from the PIL. For the events on June 21 and 22, the field lines anchored near the PIL are inverse-S-shaped and graze the PIL. Indeed, we note little difference in the observed EUV morphology with the core field. The northern sigmoid elbow in all the cases could be related to a high-lying potential-like arcade. The southern elbow seems to be constituted of a continuity of field lines belonging to both a low-lying core field and a high-lying arcade to the leading polarity.

BP separatrix is a common topological feature in sheared bipolar regions, where the buildup of FR begins with the appearance of BP (Titov & Démoulin 1999; Aulanier et al. 2010). In Figure 6, the field lines along the PIL are displayed in a close view for BP topology. The structure for the event on June 21 clearly show BP separatrix field lines. Field lines surrounding the BP separatrix are a combination of inverse-J and -S shaped field lines. A prominent dip tangentially touching the magnetogram level is displayed in the perspective view in the top right panel of Figure 6 for event 2. A similar topology is evident for events 3 and 4. In the case of event 4, the field line dips are not touching the magnetogram level ($z_{\rm dip} \simeq 0.2$ Mm above this level) so in this case a BP region is not present at the photospheric level. Still, the inverse-S shape for the field lines is clear. Notedly, these BP/dip locations move southward in time.

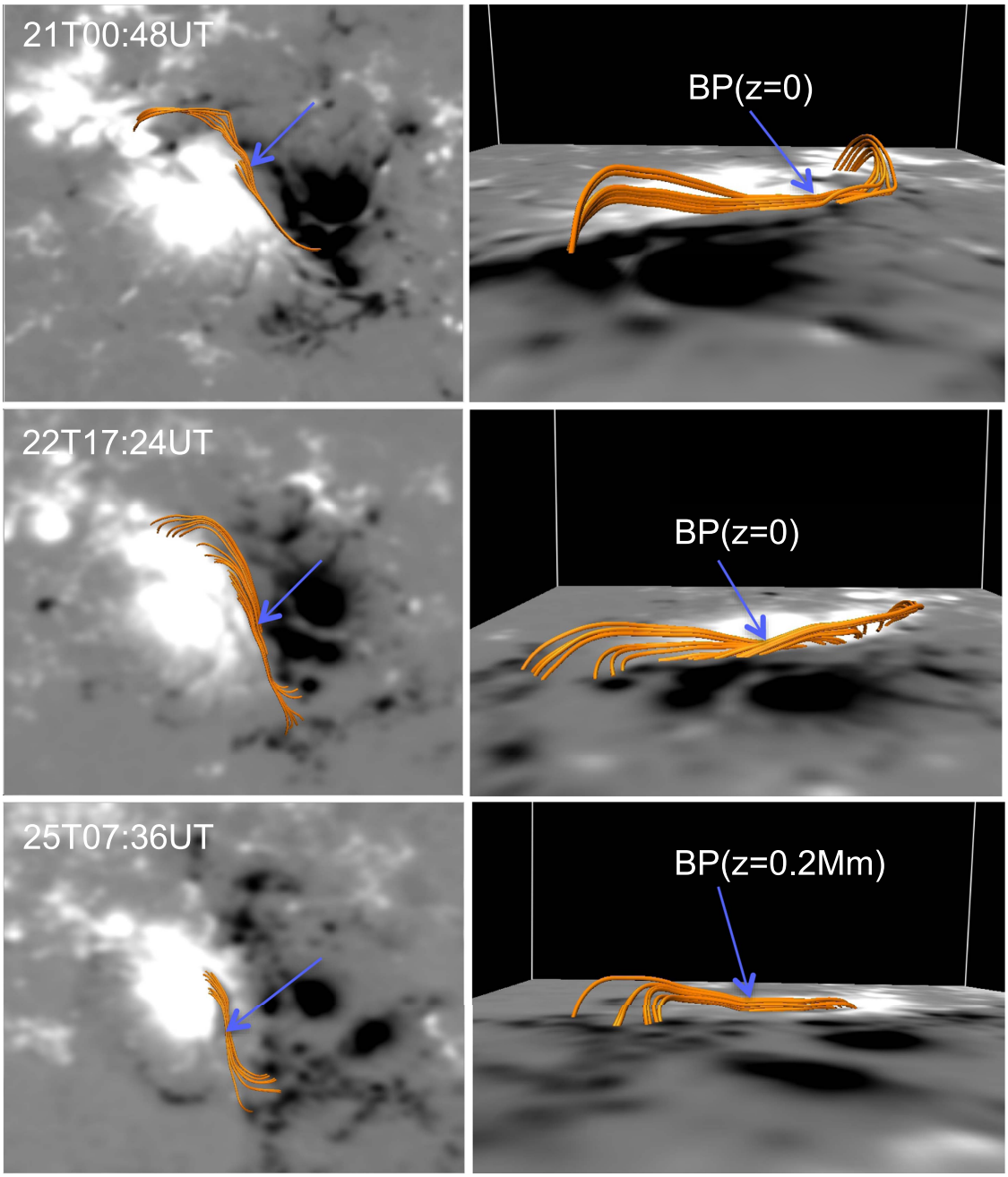

Figure 6. NLFFF structure in the inner core evidencing the BP separatrix topology. Left column: top view of field lines plotted on B_z maps. These field lines are a combination of double inverse-J and -S shapes along the PIL. Right column: perspective view of the same field lines having prominent dips touching the photosphere tangentially. Arrows point to the field line dips near to the surface ($z = 0$). This kind of topology is suited for flux cancellation reconnection of inverse-J-shaped field lines to form inverse-S shaped field lines and the FR.

As is the case in AR 12371, flux cancellation is a process transforming double J-shaped field lines to an S-shaped FR (van Ballegooijen & Martens 1989; Feynman & Hundhausen 1994) and is associated with the formation of BP with field lines tangential to the magnetogram level. This process is also expected to occur in our studied cases. Converging motions toward PIL drive the flux cancellation reconnection, resulting in a long FR field line and evidently the field lines of NLFFF along PIL include crossed inverse-J and -S. Finally, we notice that the BP locations evolve along the PIL before CMEs (not shown) so that magnetic reconnection, building the FR, is expected to occur at intermittent positions along the PIL.

BP separatrices are preferential sites of thin current sheets due to persistent photospheric shearing motions. The reconnection of field lines in these current sheets produces high temperature emission visible in hot AIA passbands. As reconnection progresses dynamically, the FR builds by added flux. In this phase, it has been shown by MHD numerical simulations that the BP bifurcates resulting in the transformation of a BP separatrix to a QSL (Aulanier et al. 2010). Then the standard coronal tether-cutting reconnection sets in below the FR, elevating its main body. Later on, the FR becomes unstable leading to the flare onset (Aulanier et al. 2010; Savcheva et al. 2012a, 2012b). The snapshot of the NLFFF

model only captures static structure, indicating BP topology i.e., the global magnetic topology evolution but not the dynamic reconnection.

Moreover, the precursor brightening (fourth row panels in Figure 2) is cospatial with the twisted core field (Figure 5). The brightening commences about an hour before the main eruption with the appearance of a hot inverse-S trace in the core, commencing the bright ribbons in the flare phase. Then, the forming FR by flux cancellation detaches the photosphere earlier on, favoring coronal tether-cutting reconnection, as in the numerical simulations reported above.

3.2. Coronal Current Distribution

Owing to time evolution of the coronal magnetic field by persistent slow photospheric shearing motions, we see a transition of the potential-like arcade in the post-eruption phase of the previous eruption to the double inverse-J-shaped sheared arcade (this transition is analyzed in Section 3.4). This process naturally builds coronal volume currents in the stressed configuration. To have more insights on the coronal current distribution, we examine direct volume rendering of $|\boldsymbol{J}|$ (not shown). Near the magnetic field concentrations, $|\boldsymbol{J}|$ is stronger since $|\boldsymbol{J}|$ is proportional to $|\boldsymbol{B}|$ along a field line in a force-free field. In particular, intense $|\boldsymbol{J}|$ are present above the inner bipolar region corresponding to the sheared/twisted field structure.

Furthermore, we vertically integrated $|\boldsymbol{J}|$ in the coronal volume and the resulting 2D maps are shown in the first column panels of Figure 7. The overall morphology of this current distribution is similar to the sigmoid observed in EUV (Figure 2). For event 4 of June 25, the $|\boldsymbol{J}|$ distribution in the core is somewhat less intense than for the two previous events. This is associated with a difference in compactness and twist of the field structure seen in panel (C2) of Figure 5.

Corresponding to before and after the eruption, in the second and third column panels of Figure 7, we display $|\boldsymbol{J}|$ obtained in vertical slice planes placed across the sigmoid. The locations of these slices are shown in the left panels of Figure 7. White curves represent B_z contours (± 80 G) extracted in the same slice. Intense $|\boldsymbol{J}|$ corresponds to the AR core that is confined below about 15 Mm. The elbow field lines (Figure 5) contribute to the distributed coronal current on either side of the PIL, whereas, above the PIL, the intense current concentration corresponds to the twisted core field.

The smaller height of coronal current in the June 25 panel likely indicates a less stressed field owing to a less compact sheared core as seen in Figure 5 (bottom row). These results delineate that the pre-eruption configuration comprises a sheared/twisted core with intense coronal electric currents above the PIL. For events 2 and 3 (top and middle rows), the electric current is more concentrated before than after the eruption. After the eruption, in the last column panels, the coronal current is less dense due to expansion of the core field.

3.3. Field Line Twist Maps

Given the 3D field distribution, one can calculate the twist number for each field line (Berger & Prior 2006; Inoue et al. 2011; Liu et al. 2016)

$$T_{\rm w} = \int_L \frac{\mu_0 \boldsymbol{J}_{||}}{4\pi B}\, dl = \int_L \frac{\nabla \times \boldsymbol{B} \cdot \boldsymbol{B}}{4\pi B^2}\, dl. \quad (1)$$

Here the twist is related to the parallel electric current given by $\boldsymbol{J}_{||} = \frac{\boldsymbol{J}\cdot\boldsymbol{B}}{|B|}$ and the line integral is along the selected magnetic field line of length L. If the magnetic field is force-free, $\nabla \times \boldsymbol{B} = \alpha \boldsymbol{B}$, then $T_{\rm w} = \frac{1}{4\pi}\int_L \alpha\, dl = \frac{\alpha L}{4\pi}$ since α is constant for each individual field line. A 4π factor in the denominator includes a factor that converts radians into turns and a factor (2) relating local twist (radians per unit length) with α (Longcope et al. 1998). In the extrapolation, the magnetic field is not exactly force-free, so we rather perform the integration with $\nabla \times \boldsymbol{B}$ within the integral. $\boldsymbol{B}$ and $\nabla \times \boldsymbol{B}$ are computed at any point in the volume by tri-linear interpolation. Then, the line integral is carried out by a five-point Newton–Cotes formula using the procedure `int_tabulated.pro` available in IDL. For a finer structure of T_w distribution, the field line integration is performed on a grid of spatial resolution double that of the extrapolation grid. The field lines, that reach one lateral or top boundary, are assumed to be open, and they are set with a zero value of $T_{\rm w}$.

The resultant $T_{\rm w}$ maps at the times before the onset of CMEs are displayed in the left column panels of Figure 8. We find that the field line twist magnitude does not exceed 1.1 turns across the maps at different times. Therefore, we scale the maps within ± 1.1 turns on a blue–red color map. The central core has always negative values of $T_{\rm w}$ ranging from -1.0 to -0.4 turns. In all cases, a highly twisted core, surrounded by $T_{\rm w}$ values with opposite signs, is observed.

For a more quantitative analysis, we choose a smaller rectangular region surrounding the core of the sigmoid for the three events (its extension is shown in the central left panel of Figure 8), and perform a histogram analysis of $T_{\rm w}$ at pixels with $|B_z| > 120$ G. Within this region, the fraction of pixels having more than one turn is 1.4%, 1.2%, and 1.46%, respectively, before these successive CMEs. Similarly, the fraction of pixels with $0.5 < |T_{\rm w}| < 1$ turn is still small since it is limited to 11.8%, 15%, and 12%, respectively, of the total number of pixels with $|T_w| > 0$ within the selected rectangular region.

We compare the above results with the ones obtained for another AR, where twisting motions were analyzed (AR 10930 Inoue et al. 2011). The fraction of pixels in the above two intervals of twist is 5% and 40%, respectively. Therefore, it appears that rotational flux motions are more efficient in injecting twist and helicity than shear and converging motions, as expected. Furthermore, according to Török et al. (2004), the critical twist to destabilize the ideal MHD kink modes in an anchored magnetic loop is about 1.75. Therefore, the observed low twist distribution in the studied AR suggests that the kink instability is not a relevant process to trigger these eruptions.

The right column panels of Figure 8 show histograms of T_w, where each panel shows a variation of T_w distribution during the CME eruption. To show how T_w varies, we compute T_w at two epochs before eruption and one epoch after eruption and plot it in different colors (the blue histogram is after eruption). Note that the asymmetric distribution is a signature of dominant negative twist in the rectangular region corresponding to core flux. In all cases, the occurrences in the histogram wings is lower than that before the CME. To quantify this decrease of twist owing to magnetic energy release, we count the pixels with $|T_w|$ above and below 0.3 turns and express them in terms of percentage change from higher values (>0.3) to lower values during pre-to-post-eruption evolution. At the epochs

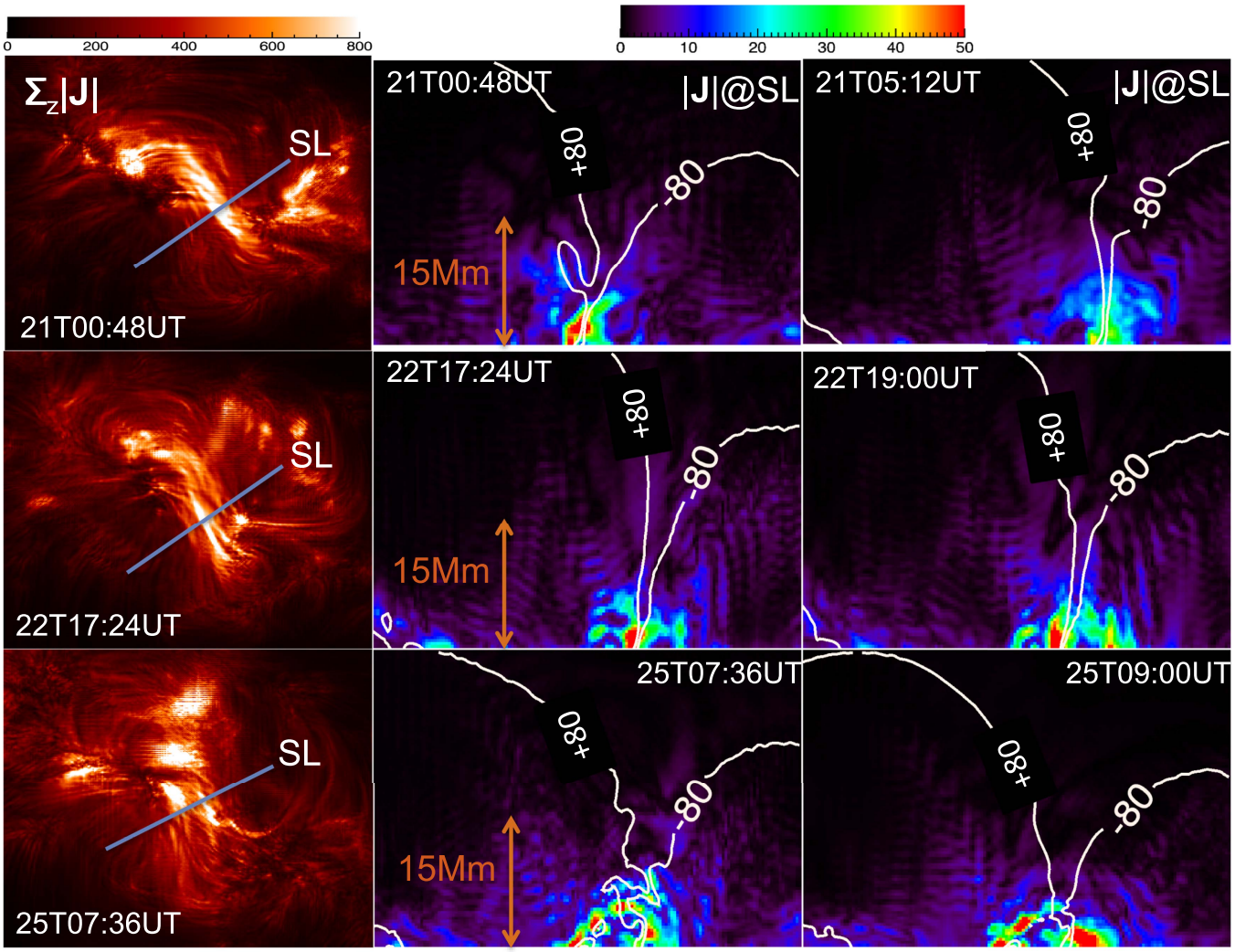

Figure 7. Current distribution just before and after three CME events. First column: vertically integrated maps of $|\boldsymbol{J}|$ scaled within the interval [0, 800]A m^{-2} (see the top color bar). They are mimicking the sigmoid observed in EUV (Figure 2). The position of the vertical slice SL, used in the right panels, is shown by a blue line. Second and third columns: electric current density, $|\boldsymbol{J}|$, in the vertical slice before and after eruption. Contours (white curves) of the vertical component B_z at $\pm$80 G are overplotted in each panel. $|\boldsymbol{J}|$ is scaled within the interval [0, 50] mA m^{-2} (see the top color bar). The strong $|\boldsymbol{J}|$ region corresponds to the sheared core field and it is surrounded by weaker currents present in the arms of the two elbow magnetic structures (Figure 5). The height scale is indicated in the panels of the middle column.

before CME eruption, the percentage of pixels above 0.3 turns is 28%, 31%, and 32%, respectively, suggesting increasing twisted flux from the first to the last event. For the three CME cases on June 21, 22, and 25, we found that the above percent of pixels decrease to 26%, 29%, and 16% (so a decrease of 2%, 2%, and 16%) respectively. The corresponding effect is seen with the histograms, where the histogram wings in the post-eruption shrink below that for pre-eruption.

3.4. Buildup of a Sheared/Twisted Core Field

As AR magnetic structure evolves, the formation of a twisted core field from an initial arcade configuration is expected under the effect of shearing and converging motions. To show this, the NLFFF reconstruction is applied at different times in the post-eruption evolution of CME1 on June 18. In Figure 9, we show magnetic structure of the AR at three instances. The first snapshot is in the relaxing phase present after the CME1. The core field has a remnant shear besides elbow field lines. In the course of further evolution driven by slow shearing/converging motions, the core field becomes twisted gradually. In particular, in the later two snapshots (pointed out by the white arrow), the core field appears more like a bundle of twisted field lines (FR). In addition, the elbow field lines appear more compact than earlier on. This buildup of twisted core is a key process of energy storage in the sigmoid structure that occurs to reform the FR from the pre-eruption arcade. This leads to the launch of the CME2 at 02:00 UT on June 21.

This development of a twisted core is further studied quantitatively by utilizing the twist T_w maps derived from the NLFFF extrapolations. Similar to an earlier section, in the last panel of Figure 9, we display histograms of T_w maps at four times in the aftermath evolution of the CME1. This time evolution of histograms delineates the transfer of pixels about the center (with $|T_w| < 0.5$) toward the wings ($|T_w| > 0.5$). The fraction of pixels with $|T_w| > 1$ turns shows a slight increase from 0.4% to 1.2% from the first instance to the last. However, corresponding to the buildup of the sheared core, the fraction of pixels with $0.5 < |T_w| < 1$ is significant and growing from 6.1% to 11.3%, so almost by a factor 2. If we instead select the interval $0.3 < |T_w| < 1$, the fractional increase becomes lower

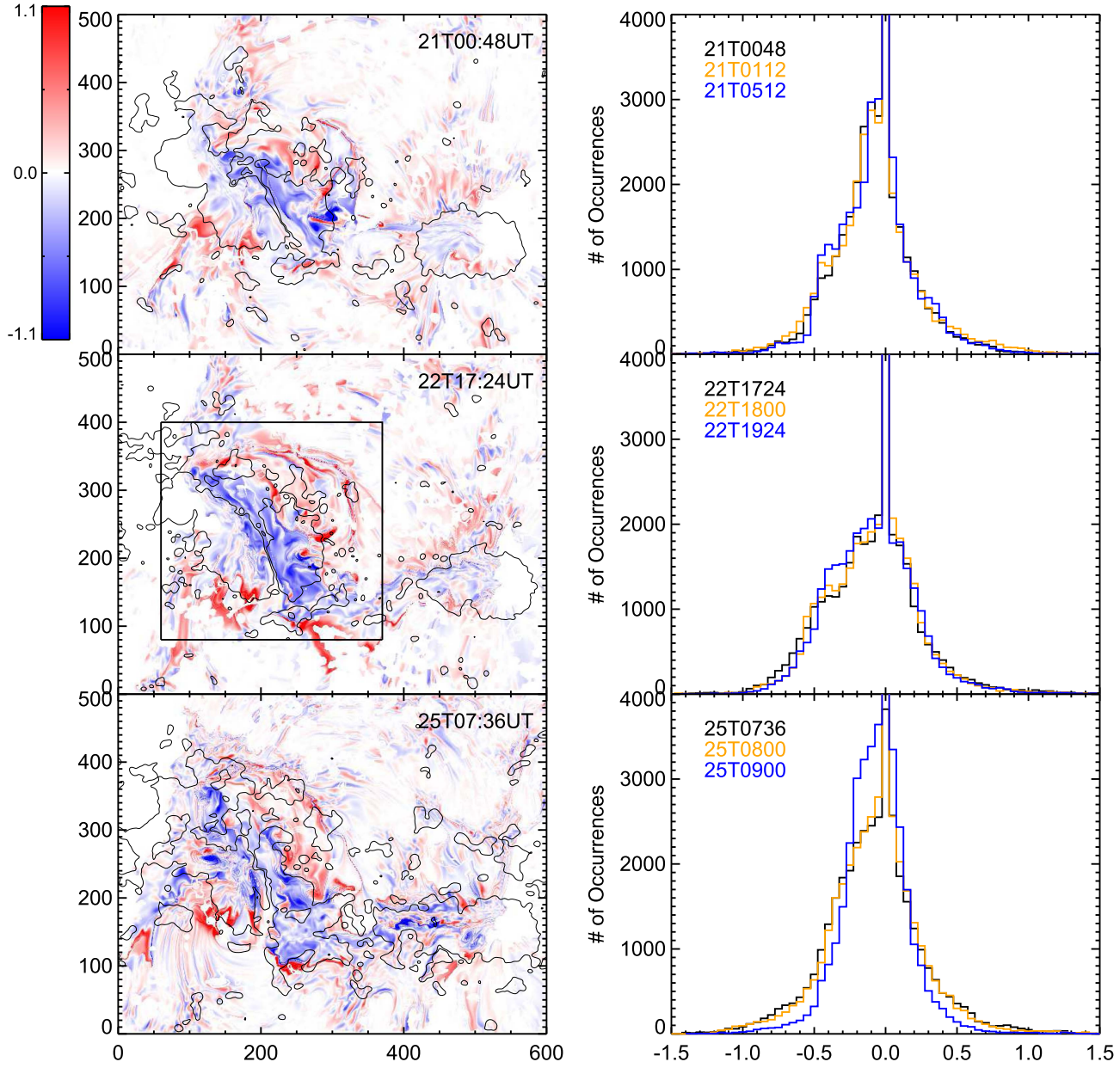

Figure 8. Spatial distributions and histograms of the field line twist (see Equation (1)). Left column: T_w distribution of AR 12371 about half an hour before the onset of CME events. Red (blue) color pixels refer to positive (negative) twist. Maps are scaled within ± 1.1 turns as shown by the blue–red color scale. Field lines with foot points around the PIL have higher negative twist. They are surrounded by a positive twisted field. A smaller rectangular region, as show in the 22T17:24 UT (second) panel, is chosen for the histogram analysis. Right column: histograms of T_w before and after the onset of each CME. The asymmetry in the distributions is due to a dominant negative T_w in the rectangular region. The histograms shrink slightly in width over time owing to the relaxation of the field during CME eruption.

as it grows from 21.2% to 29.7% from the first instance to the last one, so increasing only by a factor $\approx$1.4.

3.5. Magnetic Energy

Magnetic free energy (E_f) is a measure for excess energy available for the eruptive flares. It is estimated by subtracting the potential field energy (E_p) from the total magnetic field energy (E_t). To study the height variation of the magnetic free energy, we compute the surface integral of free energy as (e.g., Mackay et al. 2011; Vemareddy et al. 2016)

$$E_{f,s}(z) = \int_S \frac{B^2}{2\mu_0}\, dx\, dy - \int_S \frac{B_p^2}{2\mu_0}\, dx\, dy \qquad (2)$$

from the NLFFF and potential fields of the AR. For this purpose, we consider the time frames before and after the eruption. Specifically, we choose the pre-flare snapshot just before the first observed brightenings and the post-eruption snapshot at the end of the flare decay phase, ensuring the field relaxation gets captured in the vector magnetograms.

We caution that our computations of free energy estimation is subjected to errors due to projection effects, extrapolation model, and noise/bias in input observations. Moreover, implicit smoothing in the preprocessing procedure also contributes to the underestimation of the actual coronal free energy content.

During the three CME cases, the plots in Figure 10 delineate that most of the coronal free energy is contained below 20 Mm

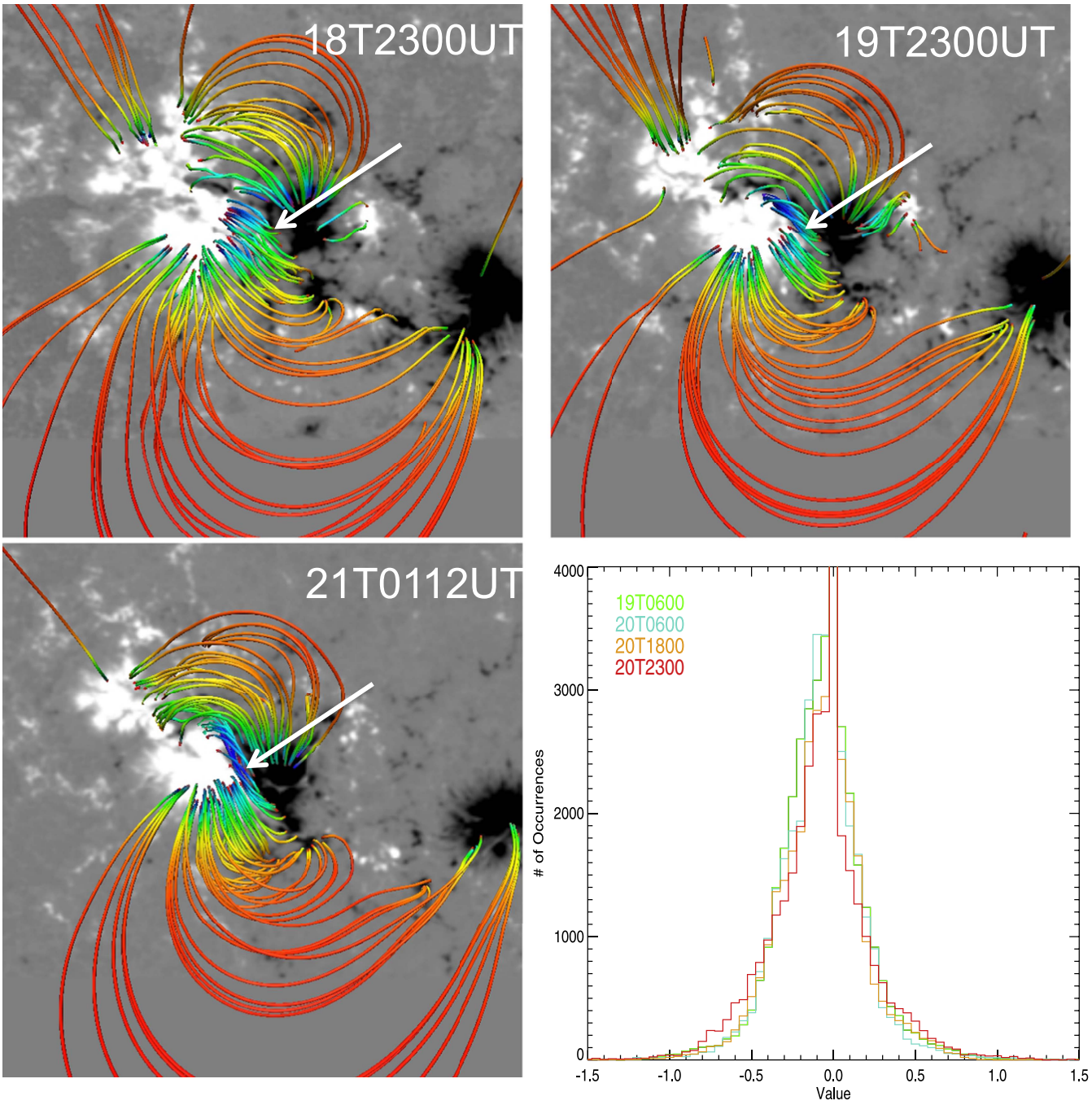

Figure 9. Development of the twisted core field by shearing motions over two days of quasi-static evolution after CME1. Image panels: NLFFF field lines are overplotted on magnetograms in the post-eruption evolution of first CME (starting at 17:24UT on June 18) and before the second CME (starting at 02:30UT on June 21). The first time is just after CME1 and the following occurances are separated by about one day. Arrows point to the buildup of the twisted core field. Field lines are color coded (blue and red): ∼1200 (2)G) with the horizontal field strength in height. Bottom right panel: histograms of T_w (Equation (1)) at four different times. It shows increasing wings corresponding to the development of a twisted core field.

and $E_{f,s}$ is maximum a low height, below 5 Mm. This energy is related to the coronal electric current distribution depicted in Figure 7. $E_{f,s}$ decrease for event 2 is small, while for events 3 and 4 the decrease of $E_{f,s}$ is significant in the range 10–30 Mm. Only in event 3 is an increase of $E_{f,s}$ present at low heights.

In Table 1, the global energies for all three CME events are reported. In each case, the time is considered just before and after the flares as above. E_p and E_t are of the order of 10^{33} erg, which is the typical energy content of large ARs (e.g., AR 12192 Jiang et al. 2016b). From events 2 through 3, E_p drops gradually. This is consistent with the photospheric magnetic flux, which is decreasing both by dispersion and by cancellation at the PIL. A decreasing E_p with reducing AR flux content is also observed in AR 11283 in the study by Jiang et al. (2014). In all events, the potential energy is almost the same before and after (Table 1) as expected because of the small observed evolution during the events of the vertical field component at the photospheric level. The magnetic energy available for an event, which is converted, e.g., as kinetic, thermal, and radiative energies, is mostly the difference of

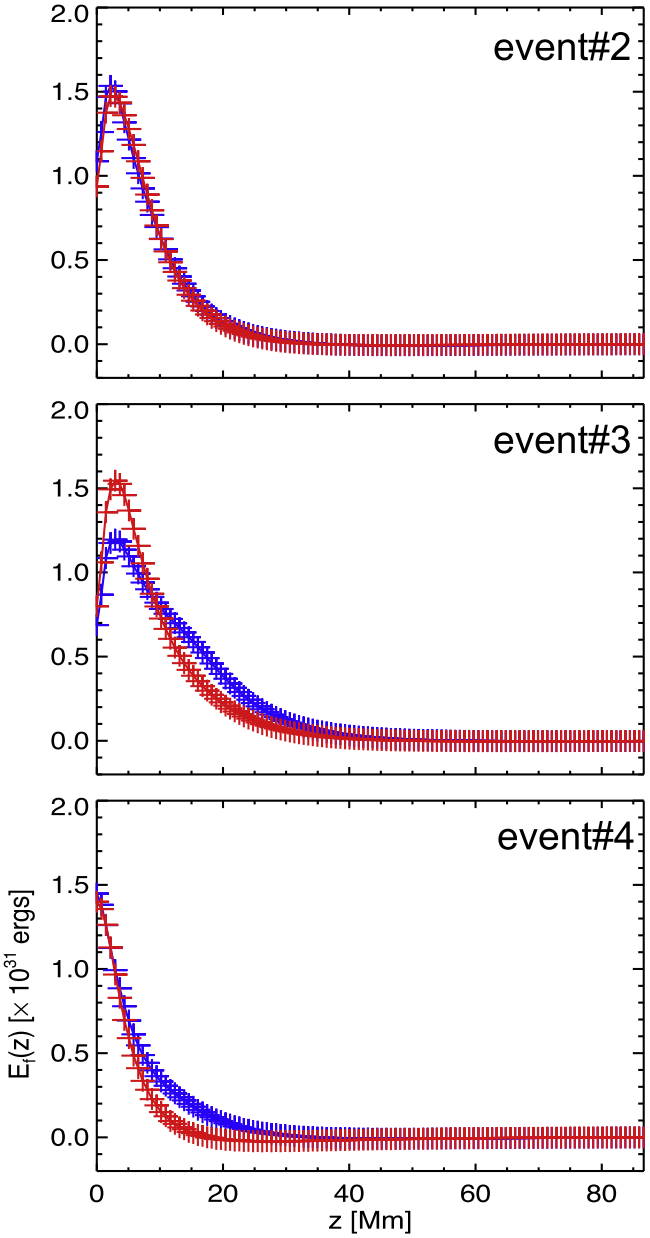

Figure 10. Free energy $E_{f,s}$, Equation (2), in horizontal planes as a function of height (z, in Mm). Blue (red) curve represents $E_{f,s}$ before (after) eruption (Table 1). Most of the free energy is located below 20 Mm. On average, the post-eruption curves are below pre-eruption curves, indicating that, as expected, $E_{f,s}$ drops through the CME eruption.

Table 1
Magnetic Energy in Units of 10^{32} erg before and after Each CME Eruption in AR 12371

Event (Time)	E_p	E_t	E_f
CME2(2015 Jun 21T00:48 UT)	26.25	28.39	2.14
CME2(2015 Jun 21T04:00 UT)	25.97	28.64	2.09
CME3(2015 Jun 22T17:24 UT)	21.54	24.19	2.64
CME3(2015 Jun 22T19:24 UT)	21.75	24.23	2.47
CME4(2015 Jun 25T07:36 UT)	22.58	24.03	1.44
CME4(2015 Jun 25T09:00 UT)	22.81	23.80	0.98

Note. E_p, E_t, and E_f are, respectively, the potential, total, and free magnetic energy ($E_f = E_t - E_p$).

coronal magnetic energy between after and before the event since eruptions involve the ejection of closed magnetic structures and since the energy input by photospheric shearing motion is small compare to the energy accumulated between two events (with a constant flux rate, this ratio is the ratio of the durations, so of the order of $2/24 \approx 0.1$).

The magnetic free energy drop for the three events is 0.05, 0.17, and 0.46 in units of 10^{32} ergs, respectively, accounting for 2.3%, 6.4%, and 32% of the pre-eruption free energy. These small values are qualitatively consistent with the estimates of twist number variation in Section 3.3, where only a small number of field lines (up to 16%) show a variation of twist number corresponding to field reconfiguration.

In summary, our analysis suggests that magnetic energy is being pre-stored in the magnetic structure by gradual shearing motions around the PIL, then it is released by intermittent eruptions.

3.6. Torus Instability

To reveal the role of the background field, we also compute the decay index $n(z) = -d\log(B_h)/d\log z$, where B_h is the horizontal component of the background field and z is the height above the photosphere. Since the vertical magnetic-field component does not contribute to the inward confining force, the decay index is computed only with the horizontal components of the field. This background field strength decides the torus instability (TI) criteria. Török & Kliem (2005) proposed the value of 1.5 as a critical decay index. In fact, the critical value of n depends on a number of factors, but is expected to be in the range $1.1 \leqslant n_{crit} \leqslant 2$ (Bateman 1978; Kliem & Török 2006; Démoulin & Aulanier 2010).

In the present study, $B_h(z)$ is obtained at different spatial points located along the PIL in the inner bipolar region. Then an average value of $n(z)$ is derived corresponding to $B_h(z)$ at those points in both potential field and NLFFF (gray and black curves in Figure 11).

The theory separates the FR magnetic field from the background field and $n(z)$ is only computed from the background field. This separation is trivial because analyzed analytical models are constructed by the superposition of these two fields. However, with magnetic extrapolations there is no precise way to separate the FR field, or its associated electric currents, from the background. Then, we consider two extreme limits: all the currents are associated with the FR, so the background field is potential, and at the opposite the FR has a negligible fraction of electric currents, so the background field is the full NLFFF. These are clearly very extreme cases but we show below that the results are comparable so that we do not need to define which field is associated with the FR for this study of the decay index.

In Figure 11, we plot $n(z)$ above the z = 0 plane. B_h is also plotted (in units of Gauss) with its scale reported on the right of each panel. In all three cases, the $n(z)$ for potential field and NLFFF follows each other except for short-scale spikes in NLFFF arising due to differentiation of a more structured field. For all three cases, the characteristic curve $n(z)$ approaches the critical value, set to $n_{crit} = 1.5$, at a height between 20 and 50 Mm, indicating a favorable magnetic environment for the destabilization of the FR, then the launch of a CME when the magnetic evolution brings the FR axis to such a height. There is some height difference for n_{crit} (up to 10 Mm) for NLFFF

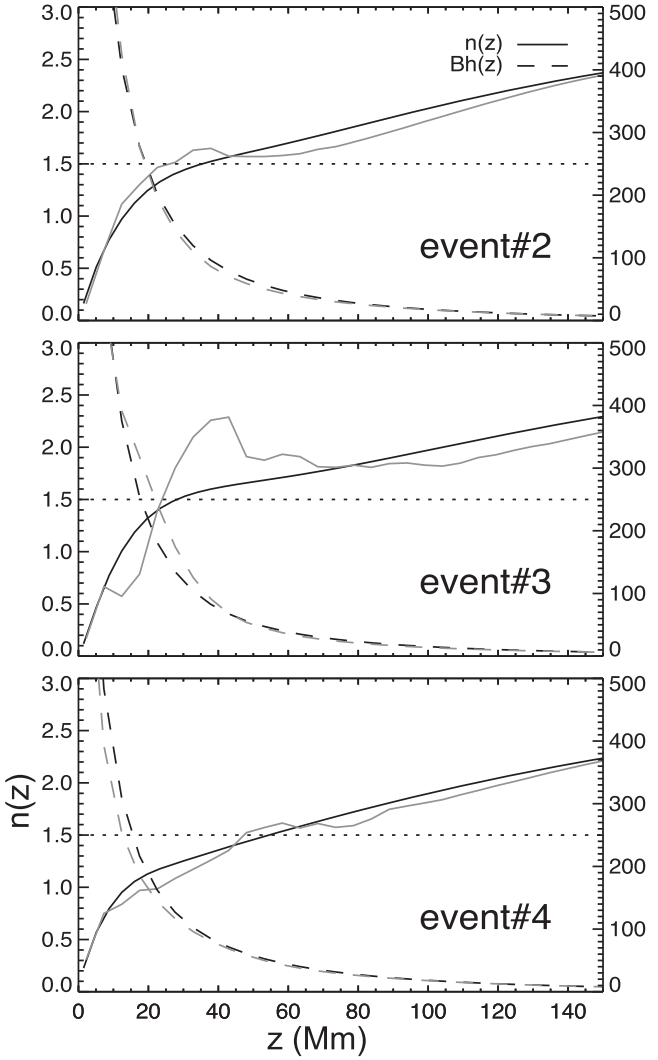

Figure 11. Decay index (n) of the background field (ordinate) as a function of vertical height (abscissa, in megameters). The black (gray) continuous curve represents the mean decay index obtained from the potential (NLFFF) field, respectively. The horizontal field strength (B_h [G]) is also plotted at the same spatial locations with dashed lines within a range between 0 and 500 G (see the scale located on the right side of the panels). The dotted horizontal line indicates the critical value of $n_{\rm crit} = 1.5$. For all three events, this critical value of n corresponds to a height just below or ≈40 Mm.

and the potential field, but the average critical height is around 40 Mm.

The TI domain in AR 12371 is comparable to other eruptive ARs, for instance, the flare-CME productive ARs 11158 and 11429 have TI critical heights of 42 and 34 Mm respectively (Sun et al. 2015). Note that the horizontal field at 42 Mm in these eruptive cases is ∼50 G, so smaller by a factor of four than in confined AR 12192 (230 G). ARs with failed eruptions have a distinct TI height range compared to ARs with successful eruptions. Recent observations found that the critical height for TI can be as high as 236 Mm (Wang et al. 2017). For a confined eruption studied by Guo et al. (2010), $n_{\rm crit}$ is always above 100 Mm suggesting a stronger restraining field over the FR. Similarly, the CME-less AR 12192 is found to have a stronger overlying field with a TI critical height up to 77 Mm (Sun et al. 2015). Indeed, the super AR 12192, producing large flares without CMEs, is found to have more closed field flux above than in the sheared core field surrounding the PIL (Sun et al. 2015; Jiang et al. 2016b).

4. Summary and Discussion

We study the magnetic structure of AR 12371, by modeling the coronal field with the photospheric vector magnetic field measurements, in relation to the erupting sigmoid observed successively over days. The AR coronal magnetic field is mainly driven by continued shear motions at the photospheric level, which inject helicity flux of dominant negative sign (see Figure 8 in Vemareddy 2017). Being cospatial with the sigmoid, the injected helicity flux is mostly included in the sheared/twisted field of the sigmoid. Because the coronal field cannot accommodate an indefinite accumulation of magnetic helicity, a CME is inevitable (Low 1994), then the stored helicity is partly ejected with the FR.

In the present study of the three events, the model field structure of the pre-eruptive sigmoid has a low-lying twisted core and an overlying arcade resembling the sigmoid morphology observed in coronal EUV images. The NLFFF core is dominantly embedded in a large-scale sheared arcade with the inner part along the PIL having opposite-J-shaped field lines with crossed legs. Closer and above the PIL inverse-S field lines with dips touching tangentially the photosphere are present (Figure 6). This kind of topology is a manifestation of BP-separatrix field lines formed by photospheric reconnection of opposite-J field lines and indicates the formation of weakly twisted FR at the inner core of the sigmoid embedded in the large-scale sheared arcade (Antiochos et al. 1999). As shown in previous simulations (see Section 1), a larger FR is progressively built up by reconnection at the photospheric level, then in the corona below the FR. At some point of the evolution, the FR becomes unstable, which leads to a CME.

Moreover, the NLFFF modeled structure captured major features of energy storage and a release mechanism, namely, sigmoid-to-arcade-to-sigmoid transformation, that is recurrent under continuous photospheric flux motions. Calculations of the field line twist reveal an increase of pixels (≈7% averaging over the events) with a range of field line twist ($0.3 < T_w < 1$), indicating the quasi-static buildup process of the twisted core field by slow shearing and converging motions around the PIL. Similarly, we observed a decrease of pixels within the same range of twist, which is consistent with the decrease of free energy corresponding to the field reconfiguration from sigmoid to potential-like arcade during the eruption.

The magnetic evolution in this AR is in contrast to the confined AR 12192, which has a larger helicity flux but much weaker (by a factor of 10) normalized coronal helicity content (H/Φ^2). As inferred by Vemareddy (2017), a small value of H/Φ^2 implies large flux content unrelated to the sheared/twisted part. This flux is present as an overlying flux to stabilize the FR. This is complemented by the results of $n(z)$ in the AR field. The critical height in eruptive AR 12371 is around 40 Mm, while in confined AR 12192 it is at a larger height (77 Mm, Sun et al. 2015).

The ejective nature of AR 12371 differs in some global magnetic properties with respect to those of confined eruptive ARs. The super AR 12192 is an interesting example that does not produce any CMEs, even in association with X-class flares, and therefore is a noneruptive counterpart of AR 12371. Data-driven modeling of AR 12192, performed by Jiang et al. (2016b), have shown that the AR field structure remained in the

sheared arcade configuration without forming two-J shape like and escaping FR unlike the AR case studied here.

Our analysis of observations is based on the static modeling of NLFFF of AR magnetic structure. More insights on dynamic aspects of FR formation and its lift off can be gained from data-driven MHD modeling of the AR (e.g., Jiang et al. 2012, 2016a) and would be worth further investigation.

SDO is a mission of NASA's Living With a Star Program. This work utilizes data obtained by the Global Oscillation Network Group (GONG) Program, managed by the National Solar Observatory, which is operated by AURA, Inc., under a cooperative agreement with the National Science Foundation. We are grateful to the referee's detailed constructive comments and suggestions that improved the scientific presentation of the results. P.V. is supported by an INSPIRE grant of AORC scheme under the Department of Science and Technology. The NLFFF code was developed by Dr. T. Wiegelmann of the Max Planck Institute for the solar system. We thank Jun Chen and Rui Liu of University of Science and Technology of China for a useful discussion on field line twist computation. 3D rendering is due to VAPOR (http://www.vapor.ucar.edu) software. We acknowledge the extensive usage of the multi-node, multi-processor high-performance computing facility at the Indian Institute of Astrophysics.

ORCID iDs

P. Vemareddy https://orcid.org/0000-0003-4433-8823
P. Demóulin https://orcid.org/0000-0001-8215-6532

References

Amari, T., Luciani, J. F., Aly, J. J., Mikic, Z., & Linker, J. 2003, ApJ, 585, 1073
Antiochos, S. K., Dahlburg, R. B., & Klimchuk, J. A. 1994, ApJL, 420, L41
Antiochos, S. K., DeVore, C. R., & Klimchuk, J. A. 1999, ApJ, 510, 485
Archontis, V., Hood, A. W., Savcheva, A., Golub, L., & Deluca, E. 2009, ApJ, 691, 1276
Aulanier, G., Pariat, E., & Démoulin, P. 2005, A&A, 444, 961
Aulanier, G., Török, T., Démoulin, P., & DeLuca, E. E. 2010, ApJ, 708, 314
Bateman, G. 1978, MHD Instabilities (Cambridge, MA: MIT Press)
Berger, M. A., & Prior, C. 2006, JPhA, 39, 8321
Bobra, M. G., Sun, X., Hoeksema, J. T., et al. 2014, SoPh, 289, 3549
Bobra, M. G., van Ballegooijen, A. A., & DeLuca, E. E. 2008, ApJ, 672, 1209
Canfield, R. C., Hudson, H. S., & McKenzie, D. E. 1999, GeoRL, 26, 627
Canfield, R. C., Kazachenko, M. D., Acton, L. W., et al. 2007, ApJL, 671, L81
Chae, J., Moon, Y.-J., & Pevtsov, A. A. 2004, ApJL, 602, L65
Chae, J., Moon, Y.-J., Wang, H., & Yun, H. S. 2002, SoPh, 207, 73
Démoulin, P., & Aulanier, G. 2010, ApJ, 718, 1388
Demoulin, P., Henoux, J. C., Priest, E. R., & Mandrini, C. H. 1996, A&A, 308, 643
Démoulin, P., Mandrini, C. H., Van Driel-Gesztelyi, L., Lopez Fuentes, M. C., & Aulanier, G. 2002, SoPh, 207, 87
Démoulin, P., Priest, E. R., & Lonie, D. P. 1996, JGR, 101, 7631
De Rosa, M. L., Schrijver, C. J., Barnes, G., et al. 2009, ApJ, 696, 1780
Fan, Y., & Gibson, S. E. 2004, ApJ, 609, 1123
Feynman, J., & Hundhausen, A. J. 1994, JGR, 99, 8451
Gary, G. A. 1989, ApJS, 69, 323
Gibson, S. E., Fan, Y., Mandrini, C., Fisher, G., & Demoulin, P. 2004, ApJ, 617, 600
Gibson, S. E., Fan, Y., Török, T., & Kliem, B. 2006, SSRv, 124, 131
Gibson, S. E., Fletcher, L., Del Zanna, G., Pike, C. D., et al. 2002, ApJ, 574, 1021
Green, L. M., & Kliem, B. 2009, ApJL, 700, L83
Green, L. M., Kliem, B., & Wallace, A. J. 2011, A&A, 526, A2
Guo, Y., Ding, M. D., Schmieder, B., et al. 2010, ApJL, 725, L38
Hoeksema, J. T., Liu, Y., Hayashi, K., Sun, X., et al. 2014, SoPh, 289, 3483
Hood, A. W., Archontis, V., & MacTaggart, D. 2012, SoPh, 278, 3
Hood, A. W., & Priest, E. R. 1979, SoPh, 64, 303
Hudson, H. S., Lemen, J. R., Cyr, O. C., St., Sterling, A. C., & Webb, D. F. 1998, GeoRL, 25, 2481
Inoue, S., Kusano, K., Magara, T., Shiota, D., & Yamamoto, T. T. 2011, ApJ, 738, 161
Janvier, M. 2017, JPlPh, 83, 535830101
Janvier, M., Aulanier, G., Bommier, V., et al. 2014, ApJ, 788, 60
Janvier, M., Aulanier, G., & Démoulin, P. 2015, SoPh, 290, 3425
Jiang, C., & Feng, X. 2012, ApJ, 749, 135
Jiang, C., Feng, X., Wu, S. T., & Hu, Q. 2012, ApJ, 759, 85
Jiang, C., Wu, S. T., Feng, X., & Hu, Q. 2014, ApJ, 780, 55
Jiang, C., Wu, S. T., Feng, X., & Hu, Q. 2016a, NatCo, 7, 11522
Jiang, C., Wu, S. T., Yurchyshyn, V., et al. 2016b, ApJ, 828, 62
Kliem, B., & Török, T. 2006, PhRvL, 96, 255002
Lemen, J. R., Title, A. M., Akin, D. J., Boerner, P. F., et al. 2012, SoPh, 275, 17
Liu, R., Kliem, B., Titov, V. S., et al. 2016, ApJ, 818, 148
Longcope, D. W., Fisher, G. H., & Pevtsov, A. A. 1998, ApJ, 507, 417
Low, B. C. 1994, PhPl, 1, 1684
Mackay, D. H., Green, L. M., & van Ballegooijen, A. 2011, ApJ, 729, 97
Magara, T. 2001, ApJ, 549, 608
Manoharan, P. K., van Driel-Gesztelyi, L., Pick, M., & Demoulin, P. 1996, ApJL, 468, L73
Martin, S. F. 1998, SoPh, 182, 107
McKenzie, D. E., & Canfield, R. C. 2008, A&A, 481, L65
Moore, R. L., & Roumeliotis, G. 1992, in IAU Coll. 133: Eruptive Solar Flares 399, ed. Z. Svestka, B. V. Jackson, & M. E. Machado (Berlin: Springer), 69
Moore, R. L., Sterling, A. C., Hudson, H. S., & Lemen, J. R. 2001, ApJ, 552, 833
Pesnell, W. D., Thompson, B. J., & Chamberlin, P. C. 2012, SoPh, 275, 3
Pevtsov, A. A. 2002, SoPh, 207, 111
Pneuman, G. W. 1983, SoPh, 88, 219
Priest, E., & Forbes, T. (ed.) 2000, Magnetic Reconnection: MHD Theory and Applications (New York: Cambridge Univ. Press)
Priest, E. R., & Démoulin, P. 1995, JGR, 100, 23443
Priest, E. R., & Forbes, T. G. 2002, A&ARv, 10, 313
Rust, D. M., & Kumar, A. 1996, ApJL, 464, L199
Savcheva, A., & van Ballegooijen, A. 2009, ApJ, 703, 1766
Savcheva, A. S., Green, L. M., van Ballegooijen, A. A., & DeLuca, E. E. 2012a, ApJ, 759, 105
Savcheva, A. S., van Ballegooijen, A. A., & DeLuca, E. E. 2012b, ApJ, 744, 78
Schou, J., Scherrer, P. H., Bush, R. I., Wachter, R., et al. 2012, SoPh, 275, 229
Schrijver, C. J. 2009, AdSpR, 43, 739
Schuck, P. W. 2008, ApJ, 683, 1134
Sun, X., Bobra, M. G., Hoeksema, J. T., et al. 2015, ApJL, 804, L28
Sun, X., Hoeksema, J. T., Liu, Y., et al. 2012, ApJ, 748, 77
Sun, X., Hoeksema, J. T., Liu, Y., et al. 2013, ApJ, 778, 139
Titov, V. S., & Démoulin, P. 1999, A&A, 351, 707
Török, T., & Kliem, B. 2005, ApJL, 630, L97
Török, T., Kliem, B., & Titov, V. S. 2004, A&A, 413, L27
Tripathi, D., Kliem, B., Mason, H. E., Young, P. R., & Green, L. M. 2009, ApJL, 698, L27
Valori, G., Kliem, B., & Keppens, R. 2005, A&A, 433, 335
van Ballegooijen, A. A., & Martens, P. C. H. 1989, ApJ, 343, 971
Vemareddy, P. 2017, ApJ, 845, 59
Vemareddy, P., Ambastha, A., & Maurya, R. A. 2012, ApJ, 761, 60
Vemareddy, P., Cheng, X., & Ravindra, B. 2016, ApJ, 829, 24
Vemareddy, P., & Mishra, W. 2015, ApJ, 814, 59
Vemareddy, P., & Wiegelmann, T. 2014, ApJ, 792, 40
Wang, W., Liu, R., & Wang, Y. 2017, ApJ, 834, 38
Wang, Y.-M., & Muglach, K. 2007, ApJ, 666, 1284
Wiegelmann, T. 2004, SoPh, 219, 87
Wiegelmann, T. 2008, JGRA, 113, A03S02
Wiegelmann, T., & Inhester, B. 2010, A&A, 516, A107
Wiegelmann, T., Inhester, B., & Sakurai, T. 2006, SoPh, 233, 215
Williams, D. R., Török, T., Démoulin, P., van Driel-Gesztelyi, L., & Kliem, B. 2005, ApJL, 628, L163
Zhao, J., Gilchrist, S. A., Aulanier, G., et al. 2016, ApJ, 823, 62